Journal of Luminescence 192 (2017) 608–615

Contents lists available at ScienceDirect

Journal of Luminescence

journal homepage: www.elsevier.com/locate/jlumin

Temporal dynamics of the frequency non-degenerate transient photoluminescence enhancement observed following excitation of inter-configurational $f \rightarrow d$ transitions in CaF_2:Yb^{2+}

Pubudu S. Senanayake[a], Jon-Paul R. Wells[a,*], Michael F. Reid[a], Rosa B. Hughes-Currie[a], Giel Berden[b], Roger J. Reeves[a], Andries Meijerink[c]

[a] The Dodd-Walls Centre for Photonic and Quantum Technologies, Department of Physics and Astronomy, University of Canterbury, PB 4800, Christchurch 8140, New Zealand

[b] Radboud University Nijmegen, Institute for Molecules and Materials, FELIX facility, Toernooiveld 7, 6525 ED Nijmegen, The Netherlands

[c] Debye Institute for NanoMaterials Science, University of Utrecht, P.O. Box 80000, TA 3508 Utrecht, The Netherlands

ABSTRACT

We present a detailed investigation of the dynamics of impurity-trapped excitons in CaF_2:Yb^{2+} using transient photoluminescence enhancement induced via a two-frequency, sequential excitation process employing a UV optical parametric amplifier (OPA) synchronized to an infrared free electron laser (FEL). The temporal behaviour is well approximated by a multi-level rate equation model as relaxation between excited states of the exciton as well as a small contribution from local lattice heating by the FEL which becomes evident due to the 40 cm^{-1} splitting of the exciton excited states giving rise to the transient photoluminescence enhancement itself.

1. Introduction

Rare-earth doped crystals are extensively utilised in modern technology from solid state laser systems to dosimeters for radiotherapy. This is because of their favorable optical and mechanical properties [1]. Additionally rare-earth doped crystals are useful in providing experimental tests of ab-initio theoretical calculations of complex systems, giving insight into fundamental quantum processes [2–4]. It is vital to gain an accurate understanding of the processes which govern the transitions and their energies to progress in both the industrial applications and verify fundamental theoretical calculations.

The sharp optical intra- $4f^N$ configuration transitions of rare-earth ions are well understood and accurate modeling of the energy levels has been done [1,5]. Unfortunately transitions involving excited configurations such as $4f^{N-1}$ 5d are more difficult to model, as a consequence of vibronic broadening of the spectra [6], which yields less information in comparison to intra-4*f* spectra.

Additionally excited configurations may further involve a charge transfer from the rare-earth ion to next nearest neighbour cations in the crystal. These delocalized electrons may form an exciton where the electron is loosely bound to the 4*f* hole. These impurity trapped excitons (ITEs) can also act as mediator for the relaxation of the $4f^{N-1}5d$ excited configuration forming an important intermediate state in the optical pumping cycle [2,7]. In some crystals doped with Yb^{2+} and Eu^{2+} ITEs form the lowest energy emitting state [8], resulting in a broad, red-shifted emission band [9,10]. This substantial vibronic broadening arises due to the fact that the electron-hole recombination gives a large bond length change [11]. To date, most information gathered about the low-lying energy levels and dynamics has been determined from indirect methods, such as the temperature dependence of photoluminescence and photoconductivity [11,12]. However, with a multi-wavelength excitation experiment it is possible to probe the internal structure of these rare-earth bound excitons directly.

Impurity trapped excitons are important intermediate states in the decay of $4f^{N-1}5d$ states, it is therefore vital to gain a more detailed understanding of the energy level structure and dynamics. Our previous work has successfully demonstrated a transient photoluminescence enhancement technique [13,14] for probing the nature of the ITEs. In this work we present a detailed investigation of the time domain dynamics of the CaF_2:Yb^{2+} ITE for multi-wavelength excitation which is modeled using a rate equation analysis.

2. Experiment

Single crystal calcium fluoride samples doped with 0.05 molar percent of YbF_3 were grown in graphite crucibles using the vertical

* Corresponding author.
E-mail address: jon-paul.wells@canterbury.ac.nz (J.-P.R. Wells).

http://dx.doi.org/10.1016/j.jlumin.2017.07.053
Received 1 February 2017; Received in revised form 26 July 2017; Accepted 27 July 2017
Available online 28 July 2017
0022-2313/ © 2017 Elsevier B.V. All rights reserved.

Bridgman method in a 38 kW Arthur D. Little RF furnace under a 10^{-5} Torr vacuum. The as grown crystals (which necessarily contained ytterbium ions in both their divalent and trivalent ionisation states [15]) were cut to a thickness of 1.5 mm and given a high quality optical polish.

A Quantronix TOPAS, frequency doubled optical parametric amplifier (OPA) was used to provide a 1 kHz train of 3 ps pulses at 365 nm. The Dutch Free Electron Laser (FELIX) was employed to provide an infrared (IR) probe. The FELIX pulse structure consists of approximately 6 μs macropulses having a repetition rate of 10 Hz. Each macropulse itself consists of a train of micropulses separated by 40 ns, each micropulse being several ps in duration. Band pass filters could be used for IR wavelengths up to 20 μm to eliminate higher harmonics from FELIX. The OPA is synchronized to FELIX via a master oscillator, thereby allowing the timing between the UV and IR pulses to be electronically varied. In our experiment, both beams were spatially overlapped at the sample (which was located in an Oxford Instruments variable temperature cryostat) and focused to a spot size of 100 μm giving a fluence of 0.13 J cm^{-2} for the UV pulse and from 5 to 11 J cm^{-2} for the IR pulse. The observed emission was dispersed in a TRIAX 320 scanning monochromator and detected using a C31034 photomultiplier tube (PMT).

3. Results and discussion

Under excitation with 27,400 cm^{-1} (365 nm) UV pulses, emission previously identified as originating from the Yb^{2+} ITE was observed, in agreement with Moine et al. [11]. Previous studies show that at a sample temperature of 8 K, the emission decays with a lifetime of approximately 15 ms. However, in our specific measurement, that can not be accurately verified due to the 1 kHz repetition rate of the OPA.

3.1. Temperature dependent emission spectra

The emission spectra for sample temperatures of 8 and 40 K are shown in Fig. 1. A least squares fit was carried out using a Gaussian line shape function, computing the intensity $I(\omega)$ (given in arbitrary units) as defined below:

$$I(\omega) = A_0 e^{\left(-\frac{\omega-\omega_0}{\Gamma}\right)^2} \quad (1)$$

where A_0 is the peak intensity, ω_0 the peak position and $(2\sqrt{\ln 2})\Gamma$ is the full width at half maximum (FWHM). The peak position was determined to be at 17,800 cm^{-1} at 8 K, in agreement with Moine et al. [11]. The measured spectrum is broad, with a FWHM of 3500 cm^{-1}, and featureless, as is typical of ITE emission [9,11,16,17].

As the sample temperature was increased to 40 K the emission intensity increased by a factor of 2.5, the spectral peak blue shifted by 600 cm^{-1} to 18,400 cm^{-1} and the spectral width narrowed by 300 cm^{-1} to 3200 cm^{-1}. The intensity increase is due to a thermal excitation of a higher lying energy level with a greater radiative decay rate [11]. The blue shift observed in emission is 15 times greater than the inferred state separation of 40 cm^{-1} (denoted as ϵ_{23} in what follows), indicating that a configurational change occurs between the two lowest excited states.

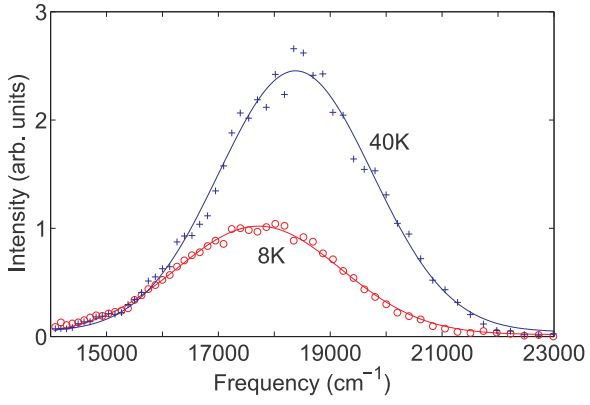

Fig. 1. Emission spectra observed from CaF_2:Yb^{2+} under UV excitation at 27,400 cm^{-1}. The solid lines are fitted Gaussian curves. The spectra have been normalized such that the peak intensity of the 8 K spectrum is 1.

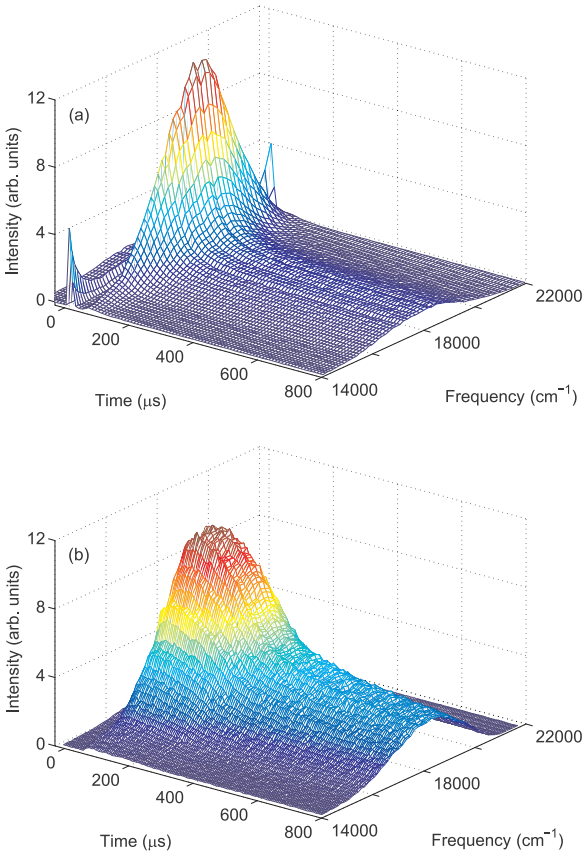

Fig. 2. Emission spectra obtained at a sample temperature of 8 K, showing the enhancement caused by the IR. The UV and IR pulses occur at $t = 0$ and $t = 100$ μs respectively. (a) Shows the response at an IR frequency of 800 cm^{-1} with the decay in enhancement occurring rapidly after the termination of the IR pulse. The peaks appearing at $t = 0$ μs are likely due to europium impurities present and the second order UV scatter. (b) Shows the response at 625 cm^{-1} excitation. A change in filters eliminated the peaks at $t = 0$ μs between (a) and (b).

3.2. Two colour excitation

Pulsed UV excitation followed by a spatially overlapped but time delayed IR pulse from FELIX leads to significant enhancement in the emission intensity from the sample, as has been described previously [13]. This phenomenon arises due to the population of excited exciton states having faster radiative decay rates than that of the exciton ground state transition. By recording these transient enhancements across the ITE emission spectrum the time–frequency plots shown in Figs. 2 (a) and (b) were obtained. These show the temporal evolution of the spectrum for IR excitation frequencies of 800 cm^{-1} and 625 cm^{-1} respectively. The UV pulse occurs at $t = 0$ μs with the IR pulse delayed by 100 μs. At $t = 100$ μs, the enhancement begins and rises, with the peak emission showing an increase by a factor of 10. It should be noted that the signal is normalized such that the peak spectral intensity prior to the onset of the IR pulse is unity. There was a change of filters between the two scans to eliminate possible emission from europium contaminants in the sample and second order UV laser scatter seen in Fig. 2(a).

The IR frequency was scanned from 1200 to 220 cm^{-1} establishing an IR excitation spectrum. A detailed analysis of its features are presented in our earlier work (see Ref. [13]). In this work we analyse and model the dynamic behaviour observed at a selection of the above IR frequencies.

The dynamic behaviour of the system is vastly different for the two IR excitation frequencies. For 800 cm^{-1} excitation (Fig. 2), the rise in the enhancement is about 12 μs, and reflects the temporal evolution of the FELIX macropulse. The enhancement decays with a time constant of approximately 40 μs and at 800 μs after the IR pulse the emission intensity falls close to the pre–IR levels.

At an IR excitation frequency of 625 cm^{-1} the rise becomes slower, increasing to approximately 20 μs and the decay time constant becomes slower at approximately 160 μs. This causes a change in the overall transient shape in comparison to excitation at 800 cm^{-1}. Additionally the emission intensity does not fall to the pre–IR level, and thus an offset appears in the spectral intensity profile. At this excitation frequency the overall emitting population fraction some time after the initial enhancement (for example from 600 to 800 μs) is greater than for the same time frame under an excitation at 800 cm^{-1}.

Fig. 3 (a) and Fig. 3(b) show the behaviour of the emission at different times in the excitation sequence for IR excitation at 800 cm^{-1} and 625 cm^{-1} respectively. The pre–IR spectrum (i.e. spectrum under UV excitation alone) is essentially identical in both cases. There is a discrepancy in the amplitude of the emission peak, however this is due to slight differences in the PMT signal amplification and different filters in use to exclude UV scatter during the two scans (Note that the spectra presented are in raw form, i.e. they have not been normalized with respect to each other, since the key comparison being made is not of the absolute spectral intensity between the two excitation regimes, but of peak position, width and their behaviour in the time domain).

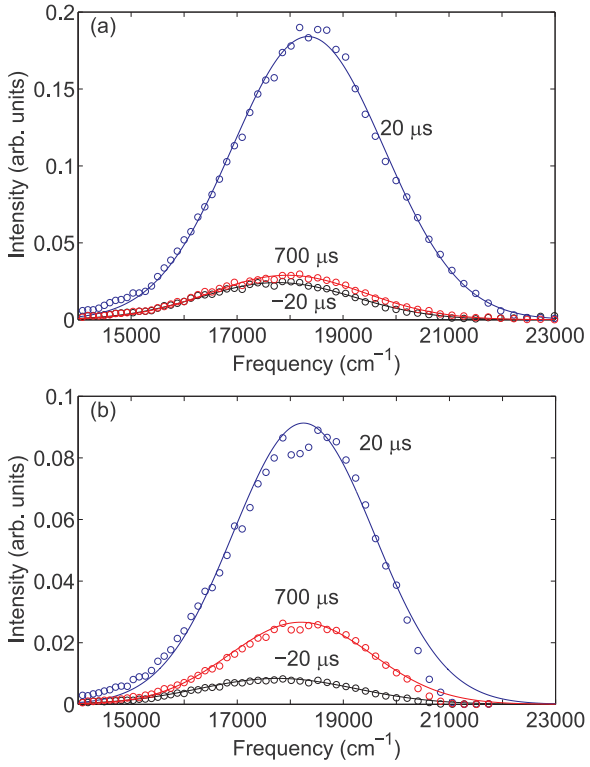

Fig. 3. The changes in the emission spectrum at 8 K for IR excitation at (a) 800 cm^{-1} and (b) 625 cm^{-1}. In each case − 20 μs is the spectrum under UV excitation only. 20 μs and 700 μs indicate the time elapsed since the IR excitation pulse was incident on the sample. Under the 800 cm^{-1} IR excitation the peak positions move significantly, first blue shifting then red shifting back to the UV only emission spectrum. Under excitation at 625 cm^{-1} the peak blue shifts, but does not return to the original position as before. The fall in intensity occurring at 21,000 cm^{-1} is due to filters used for excluding UV scatter.

Table 1
Gaussian parameter fits to the temperature dependent emission spectra from $CaF_2:Yb^{2+}$. The maximum intensity value (A_0) of the 8 K emission was fixed at 1 for the fitting. All other parameters were freely varied.

Parameter	T = 8 K	T = 40 K
A_0 (a.u)	1	2.41 ± 0.03
ω_0 (cm^{-1})	17,800 ± 14	18,400 ± 20
FWHM (cm^{-1})	3500 ± 50	3200 ± 60

Table 2
Parameters from least-squares fitting of single Gaussians to changes in the emission spectrum under UV only excitation (− 20 μs), IR excitation at 800 cm^{-1} after 20 μs and 700 μs.

Parameter	− 20 μs	20 μs	700 μs
A_0 (a.u)	0.0242 ± 0.004	0.1841 ± 0.003	0.0289 ± 0.006
ω_0 (cm^{-1})	17,800 ± 60	18,340 ± 40	17,900 ± 50
FWHM (cm^{-1})	3500 ± 80	3300 ± 30	3500 ± 50

By fitting a single Gaussian to each spectrum (as was done in Section 3.1), we extract the peak positions and widths at the different time points along the excitation sequence. The parameters extracted from these fits are presented in Tables 2 and 3.

For 800 cm^{-1} IR excitation (Fig. 3(a) and Table 2) at t = 20 μs the peak has blue shifted by 540 cm^{-1} (from 17,800 to 18,340 cm^{-1}) and narrowed by 300 cm^{-1} (from 3500 to 3200 cm^{-1}). The blue shift and the change in spectral width is in agreement with the shift and narrowing observed when the sample was heated to 40 K (comparing the parameters presented in Tables 1 and 2). Thus the IR excitation at 800 cm^{-1} is likely placing population into the first excited state. Fig. 4 shows the spectral evolution as time progresses. The return of the spectrum to the pre–IR spectrum in both peak position and width,

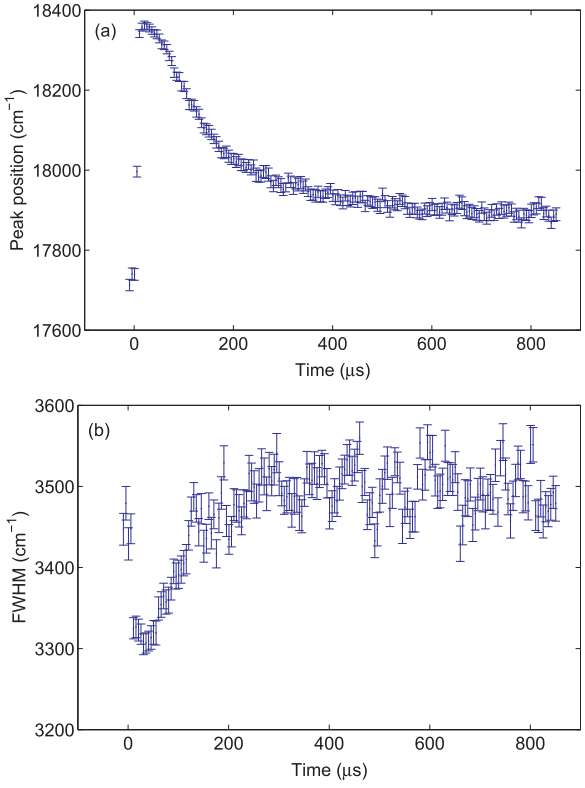

Fig. 4. The evolution of the emission spectrum at 8 K for IR excitation at 800 cm^{-1}, where the IR pulse occurs at t = 0 μs. (a) Shows the change in peak position and (b) shows the change in the full width at half maximum.

Table 3
Parameters from least-squares fitting of single Gaussians to changes in the emission spectrum under UV only excitation (– 20 μs), IR excitation at 625 cm^{-1} after 20 μs and 700 μs.

Parameter	– 20 μs	20 μs	700 μs
A_0 (a.u)	0.00840 ± 0.0002	0.0941 ± 0.004	0.0267 ± 0.006
ω_0 (cm^{-1})	17,800 ± 60	18,300 ± 100	18,200 ± 60
FWHM (cm^{-1})	3500 ± 80	3100 ± 150	3200 ± 100

indicates that the excited state emission has essentially terminated whilst the ground state transition remains observable. There is a slight difference in peak position and width, probably due to residual excited state emission.

For IR excitation at 625 cm^{-1} (Fig. 3 (b) and Table 3) the emission peak blue shifts by 500 cm^{-1} (from 17,800 to 18,300 cm^{-1}) and narrows by 400 cm^{-1} (from 3500 to 3100 cm^{-1}) at $t = 20$ μs, in agreement with the shift and narrowing observed when the sample is heated to 40 K. The spectral behaviour is also similar to that observed for IR excitation at 800 cm^{-1} and the fitted parameters are in agreement (compare Tables 2 and 3). However at $t = 700$ μs the behaviour differs from the spectrum obtained for excitation at 800 cm^{-1}. The spectrum does not evolve back to the pre–IR spectrum, instead it slowly decays, while retaining both peak position and width, indicating that the excited state emission remains dominant. The evolution of the peak position and width are shown in Fig. 5.

These results suggest that infrared excitation at 625 cm^{-1} causes a change that is long lived in comparison to the decay observed for excitation at 800 cm^{-1}. A possible explanation is that the IR is causing local heating through absorption of the IR radiation by the lattice, given that the IR absorption at 600 cm^{-1} is greater than at 800 cm^{-1} [18].

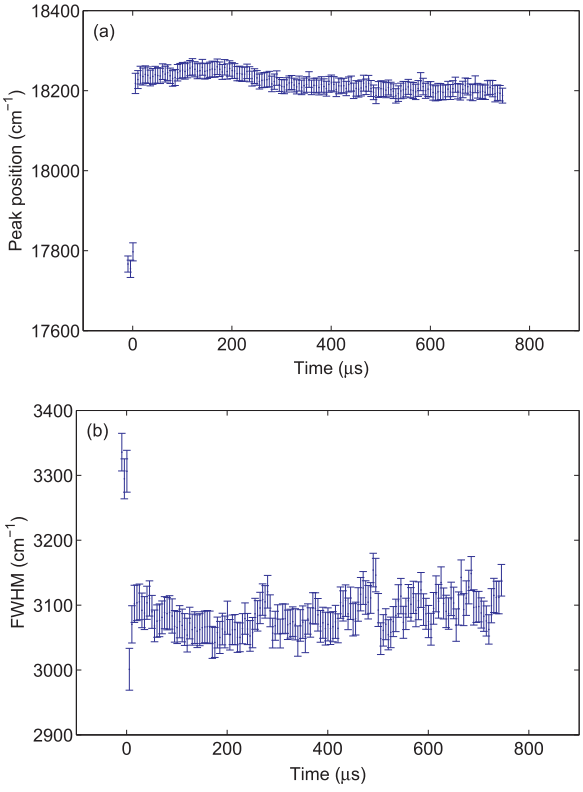

Fig. 5. The evolution of the emission spectrum at 8 K for IR excitation at 625 cm^{-1}, where the IR pulse occurs at $t = 0$ μs. (a) Shows the change in peak position and (b) shows the change in the full width at half maximum.

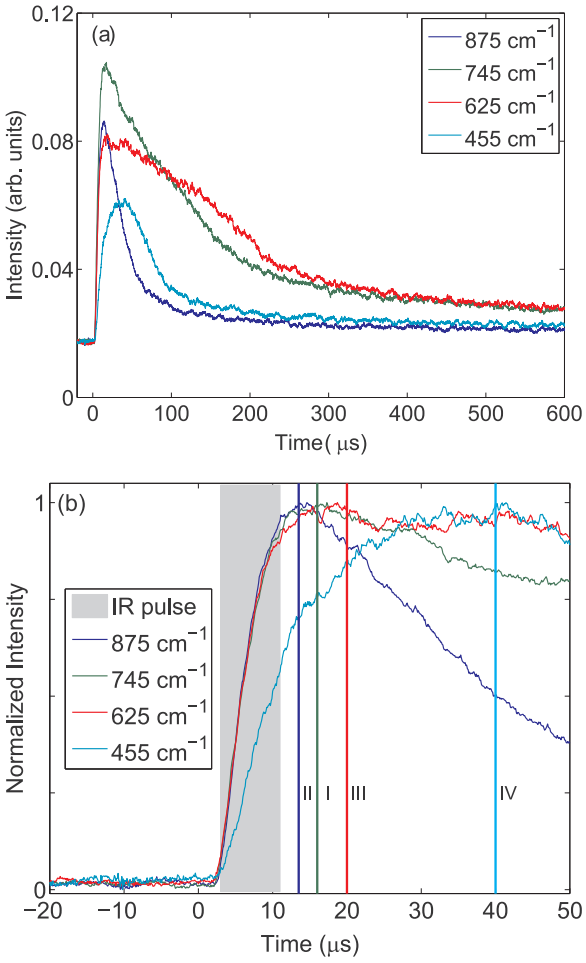

Fig. 6. (a) 8 K transient photoluminescence enhancement at four representative IR frequencies with the emission recorded at zero order. (b) The transients from (a) normalized such that their domain is [0, 1] to allow for easier comparison. The shaded area indicates the length of the IR pulse as recorded. The vertical lines indicate the instance at which the signal starts decreasing, where I is IR excitation at 875 cm^{-1}, II is 745 cm^{-1}, III is 625 cm^{-1} and IV is 455 cm^{-1}.

3.3. Dynamic response of the ITE

The IR frequency dependent dynamic behaviour is presented at four representative frequencies in Fig. 6. It is immediately obvious that there is considerable variation dependent upon the IR excitation frequency.

For excitation at 625 cm^{-1} the decay times are much longer than at any of the other excitation frequencies presented and the rise-times of the transients get progressively larger as the excitation frequency decreases towards 455 cm^{-1}. Fig. 6 (b) illustrates the rise-time trend. The shaded area indicates the length of the IR pulse and illustrates that even at an excitation frequency of 875 cm^{-1} there is a small rise in the emission beyond the termination of the IR pulse.

Drastic changes in dynamic properties, such as those above, may be interpreted as excitation into completely different ITE states displaying varying life times and excitation pathways. However considering the emission spectra presented previously (in Section 3.2), we know that the emitting state (under the excitation frequencies presented here) is predominantly the first excited state of the ITE. What is evident in examining the transient properties in conjunction with the emission spectra is that there are different dynamic mechanisms driving the population changes of the two emitting states in the ITE.

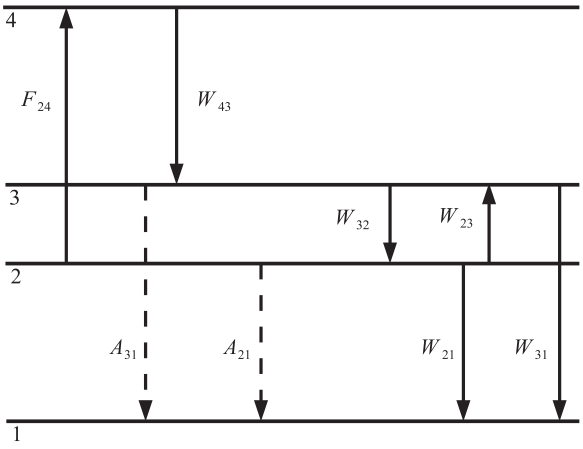

Fig. 7. A schematic representation of the rates to be used in modeling the dynamic properties of the emission observed in CaF_2:Yb^{2+}. State 1 is the $4f^{14}$ ground state. State 2 is the lowest meta-stable level and state 3 is the first excited level of the exciton. State 4 is an ITE state situated above states 2 and 3. A_{ij} denote radiative transition rates, while W_{ik} denote non–radiative transition rates. F_{24} represents the intra-exciton, IR induced transition rate.

Table 4
Parameters used in modeling of transients. The A_{ij} parameters are from previous work on CaF_2:Yb^{2+} ITE [16]. The non radiative parameters W_{21} and W_{31} have been calculated from the parameters of Refs. [11,16] for a temperature of 8.0 K. W_{32}, the non radiative relaxation rate from state 3 to 2 was determined in this work. W_{43} is assumed to be extremely fast on the time-scale of our measurements. F_{24} varies with IR wavelength and fluence.

Parameter	Value (s^{-1})	Source
A_{21}	18	Ref. [11]
A_{31}	3800	Ref. [11]
W_{21}	66	Ref. [11]
W_{31}	0	Ref. [16]
W_{32}	50,000	This work
W_{43}	Infinite	This work
F_{24}	Variable	This work

3.4. Rate equation modeling

The temporal transients can be described using a rate equation model for radiative and non-radiative transitions between the excitonic energy levels and the ground state ($4f^{14}$). Additionally the frequency dependent localized heating by the IR excitation is incorporated into the modeling. The analysis is similar to, but more detailed than our analysis for $NaMgF_3$:Yb^{2+} in Ref. [14]. The model is illustrated schematically in Fig. 7 where the energy levels are given numerical labels. The rate equations are initialized such that the exciton ground state is populated.

Previous work has determined that the ITE has two emitting states [11,16], having an energy separation of $\epsilon_{23} = 40\ cm^{-1}$. The lowest (meta-stable) state has a radiative rate of $A_{21} = 18\ s^{-1}$ whilst the upper excited state has a faster radiative rate of $A_{31} = 3800\ s^{-1}$. The lowest lying state (2) has a total relaxation rate of $66\ s^{-1}$ due to non radiative decay to the ground state. Therefore, if the first excited state (3) can be excited by infrared radiation, an increase in the emission intensity will occur. In our transient photoluminescence enhancement experiment, population of state 3 occurs through the absorption of IR photons from state 2 which populate state 3 via a higher energy state 4. Non-radiative decay from state 4 to 3 is likely to occur on a picosecond timescale.

The energy levels shown in Fig. 7 are:

1. the divalent ytterbium ground state;
2. the ground state of the impurity trapped exciton, with radiative rate A_{21};
3. the lowest excited state of the impurity trapped exciton, having an energy separation of $\epsilon_{23} = 40\ cm^{-1}$ with respect to the ground state, with radiative rate A_{31};
4. the higher-energy exciton states.

The rate equations corresponding to Fig. 7 are:

$$\begin{aligned}
\frac{dN_1}{dt} &= A_{21}N_2 + A_{31}N_2 + W_{21}N_2 + W_{31}N_3,\\
\frac{dN_2}{dt} &= -A_{21}N_2 - W_{21}N_2 - F_{24}\,f(t)N_2 - W_{23}(T)N_2 + W_{32}N_3,\\
\frac{dN_3}{dt} &= -A_{31}N_3 - W_{31}N_3 - W_{32}N_3 + W_{23}(T)N_2 + W_{43}N_4,\\
\frac{dN_3}{dt} &= -W_{43}N_4 + F_{24}\,f(t)N_2
\end{aligned} \tag{2}$$

In the equations above N_k is the population of a given state k. The function $f(t)$ is the temporal dependence pulse shape of the FELIX macropulse (IR excitation), which is measured during in course of the experiment. W_{23} is related to W_{32} via Eq. (3).

$$W_{23} = \frac{g_3}{g_2} W_{32} e^{-\epsilon/k_B T}, \tag{3}$$

where T is the temperature in Kelvin. The degeneracies of the respective levels, $g_2 = 1$ and $g_3 = 3$, are adopted from Ref. [11]. In Refs. [11,16] the rates W_{21} and W_{31} are in fact, temperature dependent. However, they may be taken as constant in the temperature range of relevance here. The magnitudes of the other parameters are presented in Table 4.

The localized temperature variation arising from absorption of the IR pulse determines W_{23} via Eq. (3). We calculate the time-evolution of the local temperature from the measured IR fluence and values available in the literature for the IR absorption, heat capacity and thermal conductivity for CaF_2. Infrared absorption is obviously strongly dependent on the exact wavelength [19,20,18] and for CaF_2 local heating can become significant below approximately $850\ cm^{-1}$. Below $460\ cm^{-1}$ (the one phonon edge of the host crystal) IR absorption becomes so strong that the fluence at the region of the sample where the IR and UV beams actually intersect is reduced by attenuation as the light propagates through the sample thickness. As a consequence, the effect of heating reduces. Additionally, the IR beam is relatively tightly focused having a 200 μm beam diameter and therefore the heating effect is spatially localized, and will not cause the overall equilibrium temperature of the sample to rise. Thus there is a sharp temperature gradient set up across the beam spot due to the Gaussian intensity profile, and this leads to dissipative cooling through heat transport. Because of this, the rapidly changing low temperature heat capacities [21] and thermal conductivities [22,23] of the sample material must also be considered.

We utilise a piecewise function to approximate the temperature change that arises from IR excitation:

$$\frac{dT}{dt} = \begin{cases} 0 & \text{pre IR} \\ E_m \dfrac{G(x,t)}{C(T)} & \text{during IR} \\ \alpha(T)\nabla^2 T & \text{post IR} \end{cases} \tag{4}$$

Here E_m is the peak energy imparted by the IR pulse to the crystal, depending on both the output power of the FEL and the IR absorption at any given frequency by the CaF_2 lattice. $G(x, t)$ is a Gaussian function describing the spatial distribution of the IR beam having a temporal profile described by $f(t)$. We take advantage of cylindrical symmetry about the beam path. The total energy delivered is converted to a temperature variation by the use of $C(T)$, the temperature dependent heat capacity of pure CaF_2.

The cooling that follows the IR pulse is modeled through solution of the heat equation in one dimension (taking advantage of the symmetry of the system). This is computed numerically, as the presence of

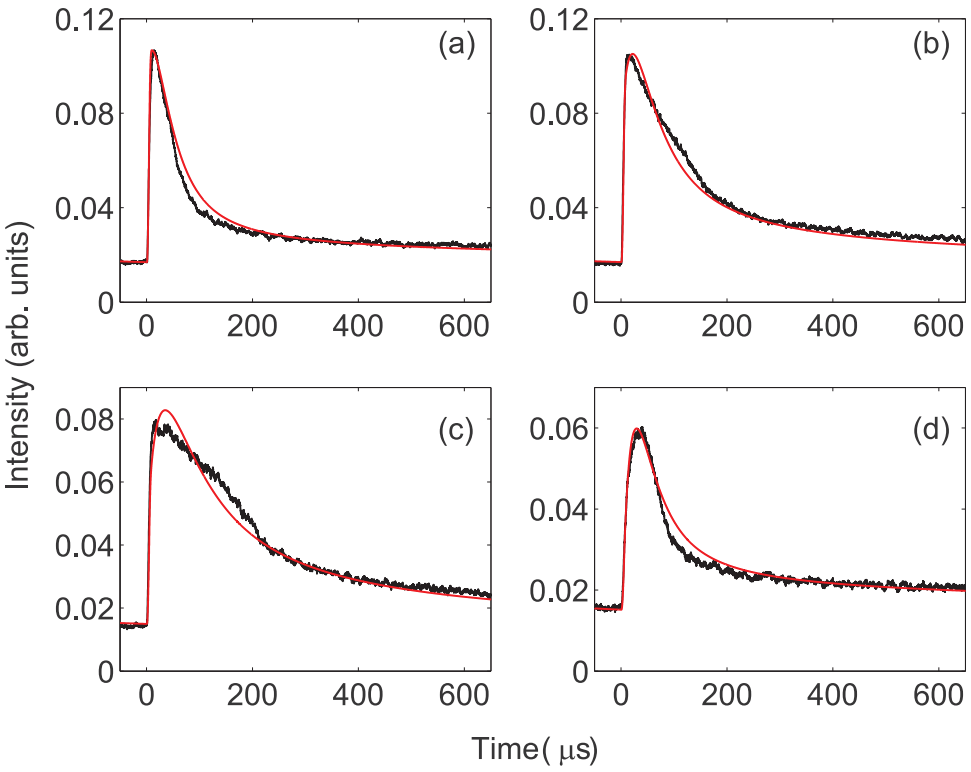

Fig. 8. The transients at different IR excitation frequencies are simulated using the rate equations discussed previously, while also taking into account the heating aspects associated with the IR radiation being absorbed into the CaF_2 lattice. The data is presented in black, while the simulated transient is presented in red. Four representative transients are displayed for excitation at (a) 833 cm^{-1}, (b) 714 cm^{-1}, (c) 625 cm^{-1} and (d) 455 cm^{-1}. (For interpretation of the references to color in this figure legend, the reader is referred to the web version of this article.)

Table 5
Parameters from least squares fitting of the IR excitation frequency dependent transients with the rate equation model presented above. F_{24} represents the intra excitonic transition rate, and is an indication of the intensity of the direct transition absorption of the IR pulse into the ITE. E_m is the total energy deposited into the lattice by the IR pulse. T_{max} indicates the maximum temperature reached by the local region under the IR induced heating. A sample temperature of 8 K was used through all the fits.

IR frequency (cm^{-1})	F_{24} (s^{-1})	E_m (mJ)	T_{max} (K)
833	13,200 ± 400	0.34 ± 0.01	15.1 ± 0.4
714	10,400 ± 500	1.02 ± 0.05	19.5 ± 0.6
625	5900 ± 300	2.5 ± 0.2	24.2 ± 1.2
455	1450 ± 70	0.25 ± 0.007	14.2 ± 0.3

$\alpha(T) \propto \frac{k(T)}{C(T)}$, the thermal diffusion coefficient which also has a strong temperature dependence, complicates the possible solutions. Here $k(T)$ is the temperature dependent thermal conductivity of CaF_2. The computed temperature T is then used to determine the relevant non-radiative rates using Eq. (3), which are then used in Eq. (2).

3.5. Determination of parameters

In Refs. [11,16] W_{32} was essentially allowed to be infinite because in those experiments, levels 2 and 3 could be described as being in thermal equilibrium. In this experiment, the FEL pulse generates a non-equilibrium situation, and the value of W_{32} is required for the modeling described above. We determine W_{32} by fitting a double exponential function of the form

$$I(t) = I_0\left[e^{-A_{31}t} + e^{-W_{32}t}\right] + y_0 \quad (5)$$

for an IR excitation frequency of 900 cm^{-1}. At 900 cm^{-1} the IR pulse does not generate significant heating of the crystal and the decay of the measured transient is largely due to the two pathways reflected in the equation. (A_{21}, W_{21} and W_{31} give negligible contributions.)

We use Beer's law to determine the relative IR fluence at the surface (facing the incoming IR beam) of the interaction volume (i.e. the volume over which the two laser beams are spatially overlapped). Integrating the IR fluence over that volume gives an approximation to the total energy deposited. Since the IR absorption is strongly frequency dependent this gives a "spectrum" of the deposited energy over the IR excitation frequencies, with the maximum heating occurring at 600 cm^{-1}.

E_m is treated as a free parameter when modeling the transients most influenced by localized heating effects (i.e. transient due to IR excitation at 625 cm^{-1}). The E_m values at other excitation frequencies can be calculated by scaling the peak value by the heating spectrum.

At any particular IR excitation frequency F_{24} can be determined through least squares fitting. As such this value serves as an indication of the relative cross-section for direct excitation of intra-excitonic states by the FEL beam. Both F_{24} and E_m are scaled according to incident IR power when conducting power measurements at a particular excitation frequency.

3.6. Modeling the IR frequency dependence

Applying the set of rate equations combined with the thermal effects already discussed the time domain behaviour across the broad excitation spectrum was fitted (i.e. to the transients presented in Fig. 6). At an excitation frequency of 833 cm^{-1} the direct intra-excitonic transitions are dominant (and this is also a value at which the emission spectra were recorded). The transients at 625 cm^{-1} excitation show the greatest potential for influence from thermal effects. Excitation at 714 cm^{-1} provides an intermediate mix of the two influences. Excitation at 455 cm^{-1} yields a transient having a long rise-time and faster relaxation dynamics. Fig. 8 shows the modeling, with the parameters presented in Table 5. The parameter F_{24} is allowed to vary across the frequency range.

It is clear that while the modeling is providing for the basic behaviour adequately, some of the fits are not perfect. This is especially so in the 625 cm^{-1} transient (Fig. 8c), where the shape of the emission enhancement is not well matched. The uncertainties of the parameters for the particular fit (Table 5) reflect the mismatch showing greater relative variation when compared to other excitation frequencies. The behaviour past 200 μs in time is well matched, with the emission offset well

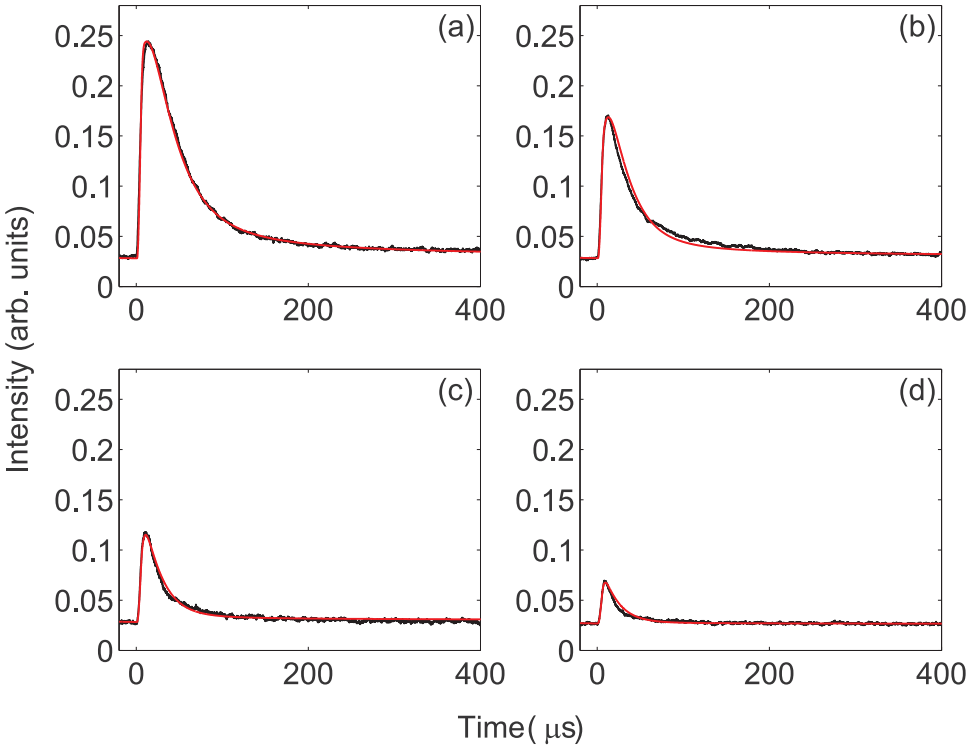

Fig. 9. The transients and the least squares fits obtained through the rate equation modeling process at different IR fluences for a frequency of 800 cm^{-1}. The data is presented in black, while the simulated transient is presented in red. Four representative transients are displayed where the IR fluences are (a) 9.6 J cm^{-2}, (b) 4.8 J cm^{-2}, (c) 3.0 J cm^{-2} and (d) 1.5 J cm^{-2}. Note that only (a) has fitted parameters, with the values for the other curves being computed from the values for (a). (For interpretation of the references to color in this figure legend, the reader is referred to the web version of this article.)

Table 6
Parameters from least squares fitting of the rate equation model to transients with varying IR excitation fluence at 800 cm^{-1} in CaF_2:Yb^{2+}.

Fluence (J cm^{-2})	F_{24} (s^{-1})	E_m (mJ)
9.6 ± 0.1	26,000 ± 800	0.70 ± 0.02
4.8	13,000 ± 400	0.35 ± 0.01
3.0	8500 ± 250	0.21 ± 0.006
1.5	4300 ± 120	0.11 ± 0.003

accounted for across the four fits. The fits at the other three frequencies where heating is not as prominent are better matched, leading to the possible implication that the modeling of the heating and heat dissipation is not entirely accurate. The large rise time observed at an IR excitation frequency of 455 cm^{-1} is due to the combination of a small F_{24} and small E_m value (see Table 5).

3.7. Modeling the IR fluence dependent behaviour

The time domain data as a function of varying IR fluence (optical density) at a frequency of 800 cm^{-1} was modeled using the same rate equation model as used in the previous sections. At maximum fluence the parameter F_{24} was allowed to vary freely and as was E_m. However E_m was initialized by a value obtained through calculation (see Section 3.5) at 0.65 mJ. Both F_{24} and E_m were scaled for lower powers and not allowed to vary. The optimised fits and the relevant data are presented in Fig. 9 whilst the fitted parameters are listed in Table 6.

Notice that because of the excitation frequency, the absorption of IR radiation into the lattice is small, thus heating is not prominent at this frequency. However due to the very low thermal capacity of CaF_2 at low temperatures, the sample experiences a temperature increase of 10 K at the IR beam spot. However the source of the emission enhancement is predominantly the intra-excitonic transition. Additionally examining the fits, it is clear that the direct transition does not saturate, as scaling the F_{24} parameter linearly with IR fluence allows for acceptable fitting to the data.

4. Conclusion

We have made an extensive investigation of the time domain behaviour of impurity trapped excitons in CaF_2:Yb^{2+} using a frequency non degenerate, transient photoluminescence enhancement technique. The temporal dynamics of this photoluminescence enhancement is well approximated by a multi-level rate equation model incorporating intra-excitonic excitation and relaxation as well as non-equilibrium lattice heating. The success in modeling the IR frequency and fluence dependent behaviour without over parameterizing, indicates that the modeling is likely valid, and that intra excitonic transition rates can be extracted from the modeling method employed.

Acknowledgements

This work was supported by the Marsden fund of the Royal Society of New Zealand via grant 09-UOC-080. The authors acknowledge the support of the Dutch FOM (Stichting voor Fundamenteel Onderzoek der Materie) organization in providing the required beamtime on FELIX. We would like to thank the FELIX staff for their assistance. P.S.S and R.H-C acknowledge the support of the University of Canterbury via Ph.D. studentships.

References

[1] B. Jacquier, G.K. Liu, Spectroscopic Properties of Rare Earths in Optical Materials, Springer Series in Materials Science, Springer, Berlin, 2005 (URL ⟨http://books.google.co.nz/books?id = HDleGQrKuEgC⟩).
[2] G. Sánchez-Sanz, L. Seijo, Z. Barandiarán, Yb-doped $SrCl_2$: electronic structure of impurity states and impurity-trapped excitons, J. Chem. Phys. 133 (2010) 114509.
[3] G. Sánchez-Sanz, L. Seijo, Z. Barandiarán, Electronic spectra of Yb-doped $SrCl_2$, J. Chem. Phys. 133 (2010) 114506.
[4] A.J. Salkeld, M.F. Reid, J.P.R. Wells, G. Sánchez-Sanz, L. Seijo, Z. Barandiarán, Effective Hamiltonian parameters for ab initio energy-level calculations of $SrCl_2$:Yb^{2+} and $CsCaBr_3$:Yb^{2+}, J. Phys.:Condens. Matter 25 (2013) 415504.
[5] W.T. Carnall, G.L. Goodman, K. Rajnak, R.S. Rana, A systematic analysis of the spectra of the lanthanides doped into single crystal LaF, J. Chem. Phys. 90 (1989) 3443.
[6] M.F. Reid, L. Hu, S. Frank, C.K. Duan, S. Xia, M. Yin, Spectroscopy of high-energy states of lanthanide ions, Eur. J. Inorg. Chem. 2010 (18) (2010) 2649–2654.
[7] M. Grinberg, S. Mahlik, J. Non-Cryst. Sol. 354 (35) (2008) 4163–4169.

[8] D.S. McClure, C. Pedrini, Excitons trapped at impurity centers in highly ionic crystals, Phys. Rev. B 32 (1985) 8465–8468, http://dx.doi.org/10.1103/PhysRevB.32.8465 (URL ⟨http://link.aps.org/doi/10.1103/PhysRevB.32.8465 ⟩).
[9] P. Dorenbos, Anomalous luminescence of Eu^{2+} and Yb^{2+} in inorganic compounds, J. Phys.:Condens. Matter 15 (2003) 2645.
[10] R.B. Hughes-Currie, A.J. Salkeld, K.V. Ivanovskikh, M.F. Reid, J.P.R. Wells, R.J. Reeves, Excitons and interconfigurational transitions in CaF_2:Yb^{2+} crystals, J. Lumin. 158 (2015) 197.
[11] B. Moine, B. Courtois, C. Pedrini, Luminescence and photoionization processes of Yb^{2+} in CaF_2, SrF_2 and BaF_2, J. Phys. 50 (15) (1989) 2105–2119.
[12] C. Pedrini, M. Joubert, D. McClure, Photoionization processes of rare-earth dopant ions in ionic crystals, J. Lumin. 125 (1) (2007) 230–237.
[13] M.F. Reid, P.S. Senanayake, J.P.R. Wells, G. Berden, A. Meijerink, A.J. Salkeld, C. Duan, R.J. Reeves, Transient photoluminescence enhancement as a probe of the structure of impurity-trapped excitons in CaF_2:Yb^{2+}, Phys. Rev. B 84 (11) (2011) 113110.
[14] R.B. Hughes-Currie, P.S. Senanayake, J.-P.R. Wells, M.F. Reid, G. Berden, R.J. Reeves, A. Meijerink, Phys. Rev. B 88 (2013) 104304, http://dx.doi.org/10.1103/PhysRevB.88.104304 (URL ⟨http://link.aps.org/doi/10.1103/PhysRevB.88.104304 ⟩).
[15] R.B. Hughes-Currie, K.V. Ivanovskikh, J.P.R. Wells, M.F. Reid, R.A. Gordon, The determination of dopant ion valence distributions in insulating crystals using XANES measurements, J. Phys.:Condens. Matter 28 (2016) 135502.
[16] B. Moine, B. Courtois, C. Pedrini, Photoconductivity and fluorescence properties of divalent ytterbium ions in fluoride crystals, J. Lumin. 48 (1991) 501–504.
[17] S. Lizzo, A. Meijerink, G.J. Dirksen, G. Blasse, On the luminescence of divalent ytterbium in $KMgF_3$ and $NaMgF_3$, J. Phys. Chem. Solids 56 (7) (1995) 959–964, http://dx.doi.org/10.1016/0022-3697(95)00035-6 (URL ⟨http://www.sciencedirect.com/science/article/pii/0022369795000356 ⟩).
[18] W. Kaiser, W.G. Spitzer, R.H. Kaiser, L.E. Howarth, Infrared properties of CaF_2, SrF_2 and BaF_2, Phys. Rev. 127 (1962) 1950–1954, http://dx.doi.org/10.1103/PhysRev.127.1950 (URL ⟨http://link.aps.org/doi/10.1103/PhysRev.127.1950 ⟩).
[19] P. Denham, G. Field, P. Morse, G. Wilkinson, P. Denham, G. Field, P. Morse, G. Wilkinson, Optical and dielectric properties and lattice dynamics of some fluorite structure ionic crystals, Proc. Roy. Soc. A 317 (1528) (1970) 55–77.
[20] M. Elcombe, A. Pryor, The lattice dynamics of calcium fluoride, J. Phys. C: Sol. Stat. Phys. 3 (3) (1970) 492.
[21] S.J. Collocott, J.G. Collins, Low-temperature heat capacity of alkaline-earth fluorides: SrF_2, BaF_2, J. Phys. C. Sol. Stat. Phys. 16 (32) (1983) 6179–6184.
[22] J.A. Harrington, C.T. Walker, Phonon scattering by point defects in CaF_2, SrF_2 and BaF_2, Phys. Rev. B 1 (1970) 882–890, http://dx.doi.org/10.1103/PhysRevB.1.882 (URL ⟨http://link.aps.org/doi/10.1103/PhysRevB.1.882 ⟩).
[23] R.O. Pohl, X. Liu, E. Thompson, Low-temperature thermal conductivity and acoustic attenuation in amorphous solids, Rev. Mod. Phys. 74 (2002) 991–1013, http://dx.doi.org/10.1103/RevModPhys.74.991 (URL ⟨http://link.aps.org/doi/10.1103/RevModPhys.74.991 ⟩).